

Overview of JT-60U Results toward Establishment of Advanced Tokamak Operation

N. Oyama 1) and the JT-60 Team

1) Japan Atomic Energy Agency, Naka, Ibaraki-ken, 311-0193 Japan

e-mail contact of main author: oyama.naoyuki@jaea.go.jp

Abstract. Recent JT-60U experimental results toward establishment of advanced tokamak operation are reviewed with emphasis on the further expansion of the operational regime of AT plasmas using improved flexibility of NBIs by the modification of power supply and on the investigation of important issues for the establishment of steady-state AT operation using new diagnostics and improved heating systems. In PS plasma, high $\beta_N H_{H98(y,2)}$ of 2.6 with $\beta_N \sim 2.6$ and $H_{H98(y,2)} \sim 1$ is sustained for 25 s significantly longer than the current diffusion time ($\sim 14 \tau_R$) without NTMs. High G -factor ($\beta_N H_{H98(y,2)} / q_{95}^2$) of 0.25 and high bootstrap current fraction (f_{BS}) > 0.43 under the ITER-like small toroidal rotation condition is suitable for ITER hybrid operation scenario. In WS plasma, high $\beta_N \sim 2.8$ exceeding the ideal MHD limit without conducting wall ($\beta_N^{\text{no-wall}}$) is sustained for ~ 5 s with RWM stabilization by a toroidal rotation at $q = 2$ surface. A combined external current drivers of negative-ion based NB and lower-hybrid waves together with high f_{BS} of 0.5 could sustain whole plasma current of 0.8 MA for 2s ($1.5 \tau_R$). In RS plasma, high $\beta_N \sim 2.7$ ($\beta_p \sim 2.3$) exceeding $\beta_N^{\text{no-wall}}$ with $q_{\min} \sim 2.4$ ($q_{95} \sim 5.3$), $H_{H98(y,2)} \sim 1.7$ and $f_{BS} \sim 0.9$ was obtained with wall stabilization. Based on PS plasma for ITER hybrid operation scenario, the high β_N of 2.1 with good thermal plasma confinement of $H_{H98(y,2)} > 0.85$ was sustained for more than 10 s at $n_e/n_{GW} > 0.7$ and $f_{\text{rad}} > 0.77$ using stored energy feedback system and radiation feedback system. Physics studies for AT plasmas, H-mode and pedestal physics, and studies on impurity transport, SOL/divertor plasmas and plasma wall interactions are also progressed. The active NTM stabilization system using modulated ECCD, which is synchronized to rotating island, has been developed and the efficiency of modulated ECCD in $m/n = 2/1$ NTM stabilization was demonstrated. The intrinsic toroidal rotation driven by the ion pressure gradient and the ECH has been confirmed and its direction is counter direction in both cases. The dedicated H-mode and pedestal experiments indicated two scalings, H-factor evaluated for the core plasma as $H_{89\text{core}} \propto I_i^{0.77}$ and pedestal width scaling of $\Delta_{\text{ped}} = 0.315 a \rho_{\text{pol}}^{*0.2} \beta_{\text{pol}}^{0.5}$. New fast diagnostics with high spatial and temporal resolutions reveals the different structure of pedestal pressure between co- and counter-rotating plasma, resulting different ELM size. The tungsten accumulation becomes more significant with increasing the toroidal rotation in the counter-direction.

1. Introduction

The development of steady-state advanced tokamak (AT) plasmas is important to realize economical fusion reactor [1]. High confinement, high normalized beta (β_N), high bootstrap current fraction (f_{BS}) and heat/particle handling are important parameters for keeping AT plasmas steadily. The current profile in AT plasmas with large f_{BS} is related to the large pressure gradient at the internal transport barrier (ITB) as shown in Fig. 1. The large $f_{BS} > 0.7$ is typically achieved in reversed magnetic shear (RS) plasmas in which a strong ITB having large pressure gradient is formed. In weak magnetic shear (WS) plasmas, a weak ITB having moderate local pressure gradient gives $f_{BS} \sim 0.5$. The flat magnetic shear with the minimum value of the safety factor (q_{\min}) slightly above 1 was achieved in positive magnetic shear (PS) plasmas with weak ITB and consequent $f_{BS} \sim 0.4$. Based on these various magnetic shear profile developed in JT-60U, it is important to investigate adequate current profile (magnetic shear profile) and pressure profile for steady state operation in terms of sustainable current profile by the bootstrap current and by the externally driven current with the neutral beam current drive (NBCD) and/or lower-hybrid current drive (LHCD), and for high β_N operation regarding to the ideal MHD limit without conducting wall ($\beta_N^{\text{no-wall}}$) and the onset of neoclassical tearing modes (NTMs). These AT research directly contribute to the development of advanced operational scenarios in ITER such as hybrid and steady-state scenarios [2].

JT-60U experiments in 2005-2006 focused on the improvement of the plasma performance and physics understanding of the parameter linkage in AT plasmas by reducing the toroidal field (TF) ripple. After the installation of ferritic steel tiles (FSTs) covering $\sim 10\%$ of the vacuum vessel surface, fast ion losses due to TF ripple were substantially reduced. Thus, high β_N plasma experiment became possible even in the large volume plasma configuration, where the large ripple losses were expected. In 2007-2008, JT-60U experiments have been focused on the further expansion of the operational regime of AT plasmas using improved flexibility of NBIs by the modification of power supply and on the investigation of important issues for the establishment of steady-state AT operation using new diagnostics and improved heating systems. With emphasis on these research activities, recent JT-60U experimental results after the 21st IAEA Fusion Energy Conference [3] are reviewed in this paper.

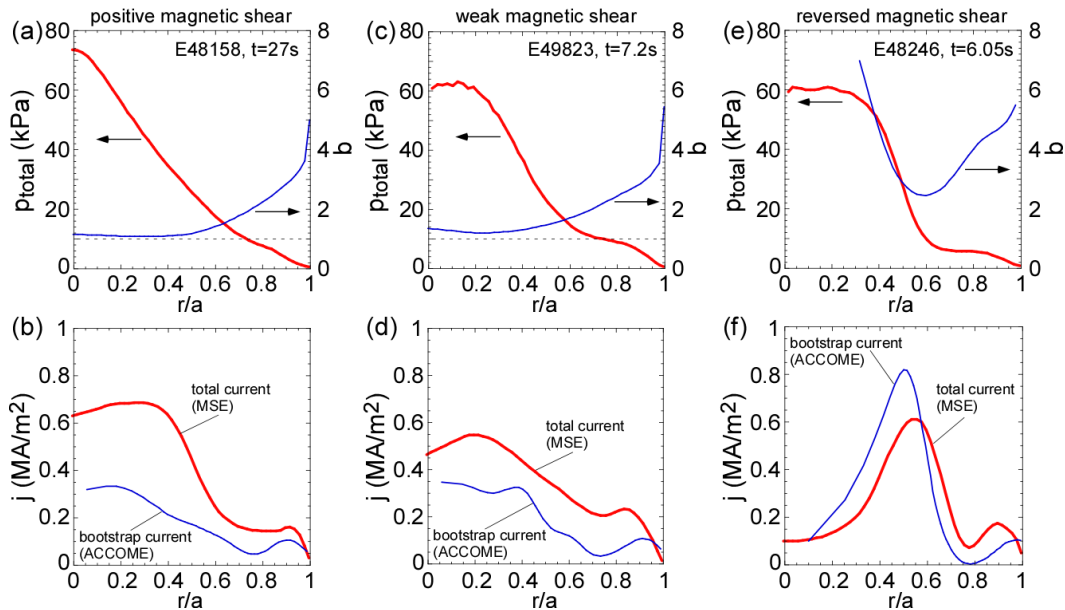


FIG. 1. (a),(c),(e) Total pressure and safety factor profile in PS (0.9MA), WS (0.9MA) and RS (0.8MA) plasmas. (b),(d),(f) Total current and bootstrap current density profile in PS, WS and RS plasmas. f_{BS} of these plasmas evaluated by ACCOME code was ~ 0.4 , ~ 0.5 and ~ 0.9 , respectively.

2. Machine Status of JT-60U

The neutral beam injection (NBI) system and electron cyclotron heating (ECH) system have been improved for 2007-2008 experimental campaign to provide further flexibility to develop AT plasmas and to investigate important physics for steady-state AT operation. In NBI system, the power supply system for three perpendicular- (PERP-) NBIs for central heating has been modified so as to extend the maximum pulse duration up to 30s. In addition to this, 29s injection of negative-ion based NBI (N-NBI) with heating power of 3 MW (85.8MJ) has been achieved [4]. Thus, the total input energy from NBIs to the vacuum vessel has been progressed up to 448 MJ. In ECH system, four gyrotrons injected high EC power of 2.9 MW for 5s (14.5 MJ). For active NTM stabilization, the power modulation technique using anode voltage control was developed to obtain high modulation frequency up to 7 kHz [5]. The system has a feature that it can trace the change of mode frequency during the discharge.

3. Extension of Operational Regime of Advanced Tokamak Plasmas

The AT tokamak research in JT-60U is focused on further extension of operational regimes with emphasis on the contribution to the ITER operational scenario such as hybrid and steady-state scenarios.

3.1. Development of Long-Pulse Hybrid Scenario with High β_N and High Confinement

The long-pulse hybrid scenario has been developed in JT-60U based on the high β_p ELMy H-mode plasma ($I_p=0.9\text{MA}$, $B_T=1.54\text{T}$ and $q_{95}=3.2$) with weak ITB. In order to extend the operational regime of hybrid discharges toward higher β_N and higher density region, the importance of the central heating to keep peaked pressure profile was investigated using new capability of long-pulse injection from PERP-NBIs for central heating. As shown in Fig. 2(a), a long-pulse hybrid discharge with high $\beta_N > 2.6$ was sustained for 28s [6, 7]. The high thermal confinement of $H_{H98(y,2)} > 1$ characterized by the peaked pressure profile shown in Fig. 2(b) was also sustained for 25 s ($\sim 14 \tau_R$, τ_R is a current diffusion time defined as $\mu_0 \langle \sigma \rangle a^2 / 12$ [8]) until $t = 29$ s with central heating shown in Fig. 2(c). The peaked profiles were appeared in both temperature and density profiles at $\bar{n}_e/n_{GW} = 0.55$. Although these hybrid discharges have highly peaked pressure profile, the pressure gradient at the mode rational surfaces at $q = 1.5$ and 2 was small enough to avoid the onset of NTMs. This NTM avoidance scenario is effective up to $\beta_N \sim 3$. The flat q profile in the core region ($r/a < 0.5$) with q_{\min} of about unity was sustained throughout the discharge and it is mainly assisted by the large bootstrap current as shown in Fig. 1(b). Thus, only infrequent sawtooth activities were observed in these hybrid discharges and their amplitude was small enough to sustain peaked pressure profile and to avoid the formation of a seed island which could trigger NTMs. The sustainable β_N in long-pulse hybrid discharges has been improved by more than 10% as shown in Fig. 2(d). It is noted that high $\beta_N H_{H98(y,2)}$ of 2.6 gives high G -factor ($\beta_N H_{H98(y,2)} / q_{95}^2$) of 0.25 and high $f_{BS} > 0.43$ under the ITER-like small toroidal rotation condition. Therefore, these long-pulse hybrid discharges are suitable for ITER hybrid operation scenario.

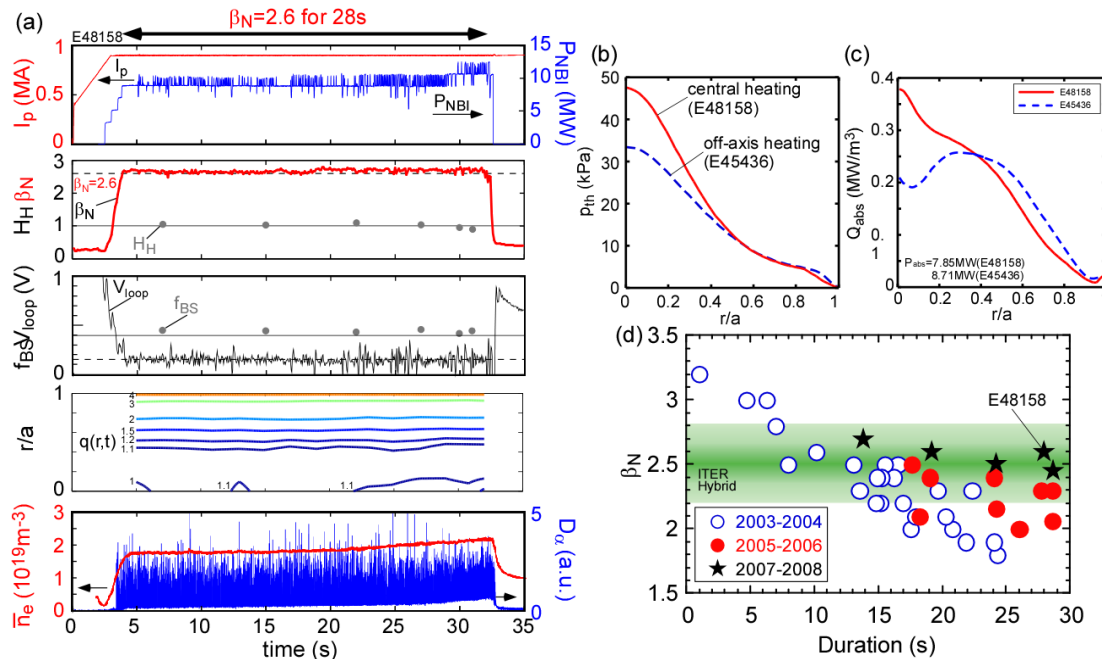


FIG. 2. (a) Waveforms of long-pulse hybrid discharge. (b), (c) Comparison of thermal pressure profile and power deposition profile between central heating (solid line) and off-axis heating (dashed line) at the same density of $\bar{n}_e/n_{GW} = 0.55$. (d) Sustained duration of high β_N plasmas.

3.2. Sustainment of High β_N Plasmas Exceeding No-Wall Ideal MHD Limit

Based on WS plasmas with weak ITB at $q_{\min} = 1.2-1.6$ shown in Fig. 1(c) ($I_p=0.9\text{MA}$, $B_T=1.44\text{T}$, $q_{95}=3.3$ and $d/a \sim 1.2$), high β_N plasmas exceeding $\beta_N^{\text{no-wall}}$ were sustained for

several seconds (longer than $\tau_R \sim 1$ s) by keeping a toroidal rotation and its shear at $q = 2$ surface so as to suppress the amplitude of the resistive wall mode (RWM) [9]. As shown in Fig. 3(a), high $\beta_N \sim 3$ was sustained for ~ 1 s and $\beta_N \sim 2.8$ was sustained for ~ 5 s. The waveforms of typical high β_N discharge are shown in Fig. 3(b). In this plasma, the plasma toroidal rotation at $q = 2$ surface was kept above the critical rotation of ~ 20 km/s in the co-direction by the torque input from co-tangential NBIs. The replacement of PERP-NBIs with N-NBIs at $t = 5.5$ - 5.9 s was also effective to keep co-rotation, because the fast ion losses originating from PERP-NBIs produce counter-torque input. According to the ACCOME calculation, the high f_{BS} of 0.46-0.5 together with the large fraction of NBCD of 0.38-0.39 provided the non-inductive current fraction of 0.84-0.89 in this WS plasma. The stability analysis by the ideal MHD stability code, MARG2D [10], indicated that $\beta_N^{\text{no-wall}}$ was ~ 2.6 and the ideal wall limit (β_N^{ideal}) was ~ 3.2 at $t = 7.2$ s. These values of $\beta_N^{\text{no-wall}}$ and β_N^{ideal} correspond to $3 l_i$ and $3.8 l_i$, respectively. With these values as a measure of

$\beta_N^{\text{no-wall}}$ and β_N^{ideal} , we can evaluate C_β defined as $C_\beta = (\beta_N - \beta_N^{\text{no-wall}})/(\beta_N^{\text{ideal}} - \beta_N^{\text{no-wall}})$. Thus, the high β_N plasma with $C_\beta \sim 0.3$ was sustained for ~ 2 s until the appearance of $m/n = 4/2$ island at $t \sim 8.2$ s, which seems to be a NTM.

In these WS discharges exceeding $\beta_N^{\text{no-wall}}$, various MHD events related to the onset of RWM have been observed. In particular, $n = 1$ bursts and slowly growing mode (precursor), which induce the reduction of the plasma rotation and consequently the onset of RWM, have often been observed. It is found that the precursor of RWM can reduce the plasma rotation shear around the $q = 2$ surface and finally trigger the RWM, as shown in Fig. 4. When the rotation shear was close to zero, the RWM can be destabilized even when the rotation speed is high enough to stabilize the RWM. Therefore, the rotational shear around the rational surface is also important to stabilize the RWM.

3.3. Sustainment of Full Current Drive Condition in Weak Magnetic Shear Plasmas

In some WS plasmas, the $\beta_N^{\text{no-wall}}$ increased together with the current penetration leading to the reduction of q_{min} . This result implies that external current drivers for off-axis current drive are needed to sustain the WS configuration. In order to establish steady-state WS scenario, WS plasma sustained by fully non-inductive current has been developed in JT-60U [6].

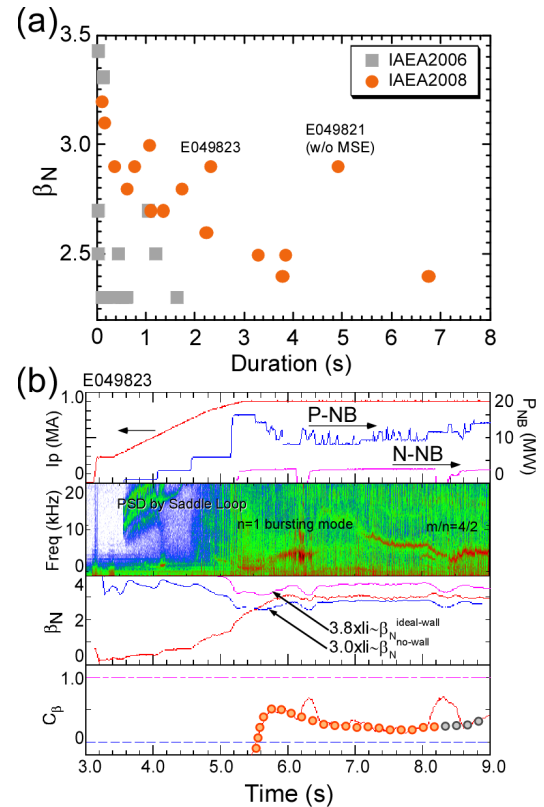


FIG. 3. (a) Sustained duration of high β_N plasmas exceeding $\beta_N^{\text{no-wall}}$. (b) Waveforms of high β_N discharge exceeding $\beta_N^{\text{no-wall}}$.

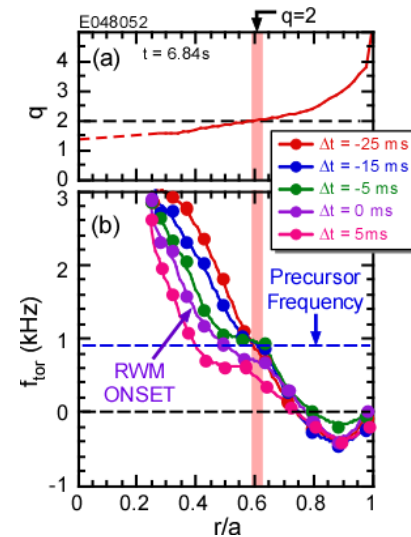


FIG. 4. (a) Safety factor profile and (b) toroidal rotation profile.

Figure 5 shows waveforms of WS plasma with $I_p = 0.8$ MA, $B_T = 2.3$ T and $q_{95} = 5.8$ under full-current drive (full-CD) condition. Pre-heating with counter-on-axis and co-off-axis NBs was applied during I_p ramp-up phase so as to form WS. After the formation of ITB by the main heating at $t = 5.2$ s, the off-axis LHCD with 1.8 MW (wave frequency 2 GHz, parallel refractive index $N_{\parallel} = 1.9$) and slightly off-axis NBCD by N-NBI with 1.2 MW (beam energy of 320 keV) were added at $t = 6$ s. Then, full-CD condition was achieved as can be seen in the surface loop voltage (V_{loop}) shown in Fig. 5(c). The V_{loop} inside the plasma became almost spatially uniform and reduced to 0 V at $t = 8.2$ s. The sustained period for 2 s corresponds to $1.5 \tau_R$. In fact, the current profile at $t = 7.5$ s and 8.0 s are almost identical, as shown in Fig. 5(d). The f_{BS} of the plasma was 0.5 and the rest of the plasma current was sustained by off-axis LHCD (0.26) and on-axis NBCD (0.24). In this WS plasma, the full-CD condition sustained for about 2 s was terminated by the notching of LH power at $t = 8.3$ s. Thus, it is expected that the q profile at $t = 8.0$ s shown in Fig. 5(d) can be sustained with off-axis current driver and high f_{BS} of ~ 0.5 .

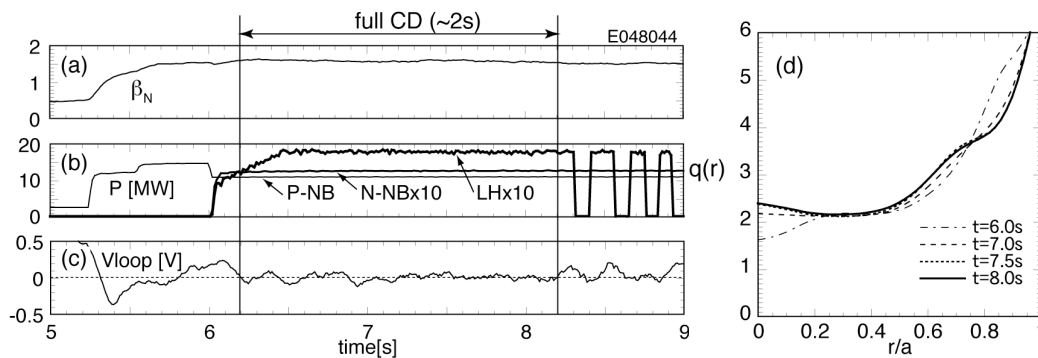


FIG. 5. Waveforms of (a) β_N , (b) injection power of P-NB (thin line), N-NB (medium line) and LH waves (thick line), (c) surface loop voltage. The full-CD condition lasts for ~ 2 s at fixed β_N . (d) safety factor profiles at $t=6.0, 7.0, 7.5$ and 8.0 s measured by the MSE diagnostics. The q_{min} and the $q(0)$ at $t=8.0$ s are 2.1 and 2.4, respectively.

3.4. Expansion of Operational Regime in Reversed Magnetic Shear Plasmas with High f_{BS}

The AT tokamak research in RS plasmas with large $f_{BS} > 0.7$ has been performed at high $q_{95} > 8$ so far. In 2008, further development to expand the operational regime of RS plasmas in terms of lower q_{95} and higher β_N exceeding $\beta_N^{no-wall}$ was performed by utilizing the wall stabilization with $d/a \sim 1.3$ [11]. Typical waveforms of the RS discharge ($I_p=0.8$ MA, $B_T=2.0$ T, $q_{95}\sim 5.3$,

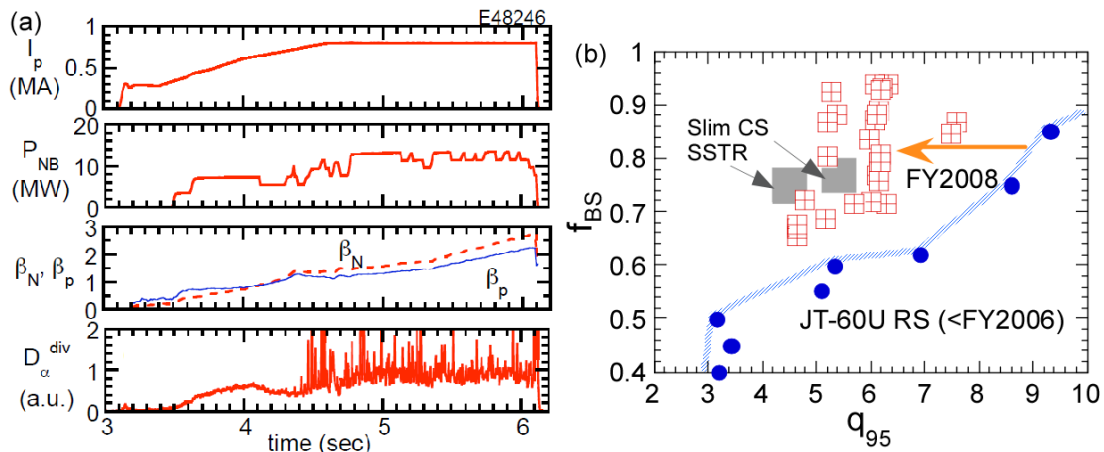


FIG. 6. (a) Waveforms of high f_{BS} discharge. (b) Operational regime of RS plasmas with high f_{BS} .

$\kappa \sim 1.5$, $\delta \sim 0.39$) with strong ITB are shown in Fig. 6(a). In this discharge, high $\beta_N \sim 2.7$ and $\beta_p \sim 2.3$ were achieved, although the plasma was terminated by the disruption at $t \sim 6.1$ s. The achieved β_N was much higher than previous experiments with $\beta_N \sim 1.7$ -2.2 in large f_{BS} plasmas. The disruption was caused at $q_{min} \sim 2.4$ (not at the integer value of q_{min}) by the RWM ($n = 1$), of which growth time is the order of the resistive wall time ($\tau_W \sim 10$ ms). The stability analysis by MARG2D code indicated that the plasma exceeded $\beta_N^{no-wall} \sim 2.0$. Moreover, high confinement enhancement factor $H_{H98(y,2)} = 1.66$ was obtained at high density regime ($\bar{n}_e/n_{GW} \sim 0.87$) attributed to both internal and edge transport barriers. The reversed q profile shown in Fig. 1(e) was formed with $q_{min} \sim 2.4$ and its location $\rho_{q_{min}} \sim 0.6$. As observed in the total current profile and bootstrap current profile shown in Fig. 1(f), high $f_{BS} \sim 0.9$ was achieved at the end of the discharge. Since tangential NBIs were used as balanced injection, beam driven current was negligible. Based on these RS plasmas, operational regime of RS plasmas with large f_{BS} and high β_N was extended towards reactor relevant low q_{95} regime as shown in Fig. 6(b). The parameters of RS plasmas close to the required values for steady-state scenarios in ITER. However, a plasma control scheme to avoid disruption (suppress the RWM) should be developed for the establishment of steady-state RS plasma operation.

3.5. Sustainment of High Density and High Radiation Plasmas with High Confinement

Reduction of heat loading appropriate for the plasma facing components such as the divertor and the first wall is also important issue for next step devices. Thus, the long-pulse high density and high radiation plasmas with good confinement has been developed based on long-pulse hybrid discharge ($I_p = 1.05$ MA, $B_T = 2.0$ T and $q_{95} = 3.6$) using impurity gas seeding [12]. The puffing rate of Ar gas was controlled by the real-time feedback system to keep the radiation from the edge region of main plasma constant. In addition to the injection of Ar gas, pulsed gas puffing of Ne gas was also applied from the divertor injector to increase the radiation at the divertor region. As the Ne puff was injected, the radiation power at the divertor gradually increased, while keeping the core radiation was almost constant. The total radiation loss fraction, $f_{rad} = (P_{rad}^{main} + P_{rad}^{div})/P_{NET}$, was achieved 0.77 at $t = 14$ s. Although the wall-pumping was not effective at $t \sim 12$ s (under wall saturated condition), the high β_N of 2.1 with good thermal plasma confinement of $H_{H98(y,2)} > 0.85$ was sustained for more than 10 s at $\bar{n}_e/n_{GW} > 0.7$ and $f_{rad} > 0.77$ using stored energy feedback system and radiation feedback system.

The species of impurity for effective cooling was also investigated as shown in Fig. 7(b). From the view point of the radiation at divertor region with lower temperature, Ne is more effective than Ar. On the other hand, Ar is better radiator for the main plasma. Thus, the combination of Ar + Ne is better way to obtain high $f_{rad} > 0.8$ while keeping high $H_{H98(y,2)}$.

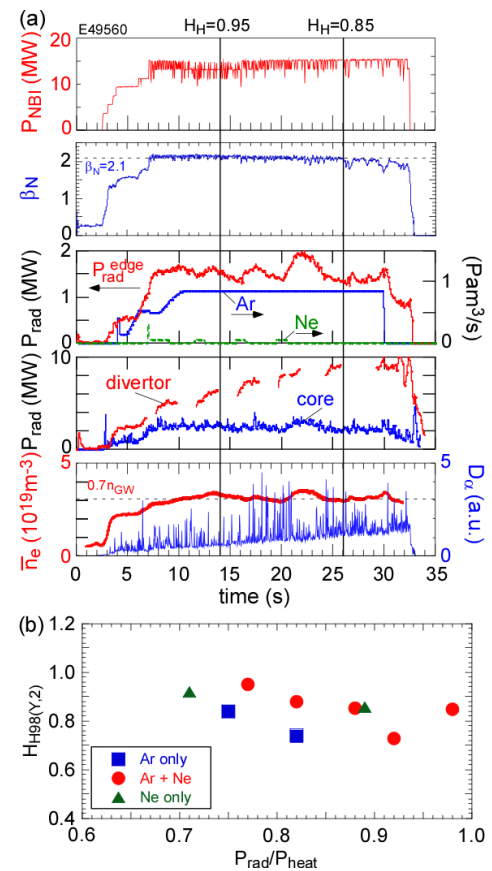


FIG. 7. (a) Waveforms of high f_{rad} and high n_e discharge. (b) H_H factor as a function of f_{rad} .

4. Progress in Physics Studies for Advanced Tokamak plasmas

Various physics researches for AT plasmas have been performed in JT-60U in order to resolve important issues for improvement of the plasma performance and better prediction of plasmas in next step device.

4.1. Active Stabilization of Neoclassical Tearing Modes

The active NTM stabilization system using modulated ECCD, which is synchronized to rotating island at ≈ 5 kHz as shown in Fig. 8(a), has been developed in JT-60U [13, 5]. The system can trace the change in the rotation speed during the stabilization. The efficiency of modulated ECCD in $m/n = 2/1$ NTM stabilization was demonstrated as shown in Fig. 8(b). The stabilizing effect of modulated ECCD near the O-point with one gyrotron was similar to the unmodulated ECCD with two gyrotrons. Figure 8(c) also shows the effectiveness of O-point ECCD. The decay time (defined by fitting the magnetic perturbation amplitude as $\exp[-t/\tau_{\text{decay}}]$ for the initial 300 ms data) reaches a minimum around -10° , which corresponds to O-point ECCD.

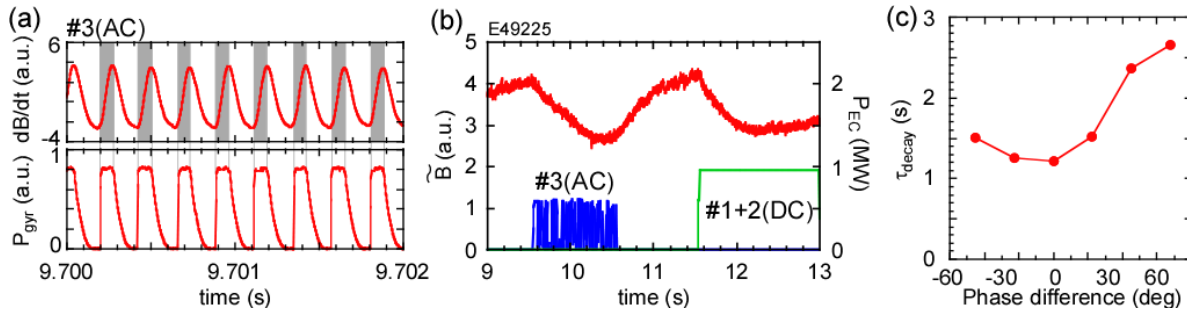


FIG. 8. (a) Magnetic probe signal and gyrotron power. (b) Time evolution of magnetic perturbation amplitude for modulated ECCD (AC) followed by unmodulated ECCD (DC). (c) Dependence of decay time of magnetic perturbation amplitude on phase difference.

The minimum electron cyclotron (EC) wave power for complete NTM stabilization of an $m/n=2/1$ mode was experimentally identified as $0.2 < j_{\text{EC}}/j_{\text{BS}} < 0.4$ for $W_{\text{sat}}/d_{\text{EC}} \sim 3$ and $W_{\text{sat}}/W_{\text{marg}} \sim 2$, and $0.35 < j_{\text{EC}}/j_{\text{BS}} < 0.46$ for $W_{\text{sat}}/d_{\text{EC}} \sim 1.5$ and $W_{\text{sat}}/W_{\text{marg}} \sim 2$ (W_{sat} , W_{marg} and d_{EC} are full island width at saturation, marginal island width to fully stabilize the NTM and FWHM of ECCD profile, respectively). For complete NTM suppression, it is confirmed that the precise alignment of the ECCD location, $(\rho_{\text{EC}} - \rho_{\text{NTM}})/d_{\text{ECCD}} \leq 0.2$, is required at $W_{\text{sat}}/d \sim 1.5$ and $W_{\text{sat}}/d \sim 3$ [13]. The modified Rutherford equation (MRE) is tested against experimental data from ASDEX Upgrade and JT-60U to obtain a common coefficient for MRE. The same analysis method to estimate the coefficient of c_{sat} for saturation phase was applied to experimental data obtained in the case of $m/n=3/2$ NTM from both devices. It is found that c_{sat} is close to unity for both devices [14]. The NTM experiments in JT-60U for this study were performed from IPP Garching using the remote experimental system developed in JAEA [15].

4.2. Studies on Internal Transport Barrier

4.2.1. Development of ITB during Formation Phase

The development of ITB in PS and RS plasmas are characterized by the evolution of the location of ITB and its strength [16]. In PS plasma with weak ITB, the ITB region expanded as the ITB location moved outward from $\rho = 0.39$ to 0.57 (ITB width $\Delta\rho > 0.2$) and the ITB

strength was moderate (~ 30 keV/m). In RS plasma with strong ITB, on the other hand, the ITB strength was larger (60 keV/m) and more localized at $\rho = 0.65$ ($\Delta\rho < 0.15$). At the beginning of ITB formation, the ITB location is far inside of the ρ_{qmin} . However, at the end of ITB formation, the ITB location reaches to the ρ_{qmin} , and the ITB location tends to keep tracking to the ρ_{qmin} . Therefore, if the ρ_{qmin} moves inward after the fully development of ITB, the ITB location also moves inward associated with the movement of ρ_{qmin} .

4.2.2. Response of ITB to External Perturbations

Responses of ITB by edge fueling of shallow HFS pellet injection and supersonic molecular beam injections (SMBI) installed in collaboration with CEA-Cadarache are investigated [17]. The ion temperature (T_i) decreases even in the central region with both pellet injection and SMBI. In the SMBI case, time evolution of T_i measured with newly installed fast CXRS system can be described by cold pulse propagation using the ion thermal diffusivity estimated from power balance analysis. By optimizing the injection frequency and the fueling depth, high confinement is sustained at high density by keeping strong ITB and enhanced pedestal pressure in the case with shallow HFS pellet injections.

Variety of T_i -ITB response is observed with central ECH in weak shear plasmas depending on the target plasmas [17]. When stiffness feature is strong in T_e profile, T_i -ITB degraded. On the other hand, T_i -ITB is unchanged or even grows, when stiffness feature is weak in T_e profile. Density fluctuation level seems to be unchanged, however, correlation length becomes longer for the degradation case and shorter for the unchanged case.

The impact of type I ELMs on weak ITB in PS plasma is also investigated. As pedestal stored energy (W_{ped}) and total stored energy (W_{tot}) increased, the location of ITB foot moved to outward and ELM affected area became wider. When the ELM affected area reaches the location of ITB-foot, the ITB radius is limited by the ELM affected area in contrast to the L-mode edge plasma. If ELM size continued to increase with increasing W_{ped} and W_{tot} , ITB was shrunk after several attacks of ELMs on the ITB foot. Thus, ELM mitigation is also important for the performance and sustainment of ITB [18].

4.3. Mechanism of Formation of Toroidal Rotation Profile and Momentum Transport

In recent experimental results, it is found that the toroidal rotation (V_t) is important for the performance of ITB and ETB, characteristics of ELM and stabilization of RWM. Thus, detailed properties of momentum transport and intrinsic rotation as the determining process of V_T were investigated in ELMy H-mode plasmas using transient analysis to evaluate the momentum diffusivity, χ_ϕ , and the convection velocity, V_{conv} , separately. The χ_ϕ evaluated at the core plasma region increases with increasing heating power and decreases with increasing plasma current. The ratio of χ_ϕ to χ_i was found to be $\sim 0.7-3$ and the ratio of V_{conv} to χ_ϕ was found to be $-2 - -0.5$ (m^{-1}). The intrinsic rotation driven by the local pressure gradient toward counter direction increased with increasing the ion pressure gradient ($\text{grad}P_i$) [19, 20].

The intrinsic rotation by ECH is also studied in plasmas with balanced NBI heating to minimize the momentum input. As shown in Fig. 9, the measured V_t in the region of $0.2 < r/a < 0.3$ was changed with ECH changed in co-direction, while one in the region $0.3 < r/a < 0.6$ changed in the counter-direction [20]. This response to ECH is determined by the combination of the momentum transport, the intrinsic rotation by $\text{grad}P_i$ and the intrinsic rotation by ECH. As for the momentum transport with ECH, it is confirmed that V_t produced

by χ_ϕ and V_{conv} in the region $0.4 < r/a < 0.7$ were not changed. The change in the intrinsic rotation by $\text{grad}P_i$ is evaluated as shown by dashed line in Fig. 9. Since the increase of counter-rotation in the region $0.4 < r/a < 0.6$ can not be explained by the change in $\text{grad}P_i$ and the momentum transport, the difference between the change in measured V_i with ECH and the change in the intrinsic rotation by $\text{grad}P_i$ shown by solid line in Fig. 9 indicated the intrinsic rotation due to ECH.

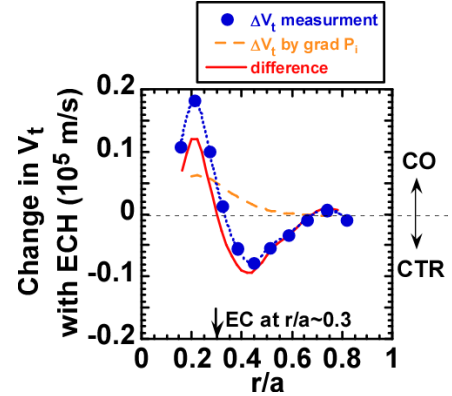


Fig. 9 Change in V_t with ECH. Dashed line shows the change in the intrinsic rotation by $\text{grad}P_i$. Solid line shows the difference in two lines, and means the intrinsic rotation by EC.

The generation of the toroidal rotation due to the radial current torque induced by the charge separation of the particle injected from NBI is studied by using one-dimensional multi-fluid transport code TASK/TX, which can evaluate $j \times B$ torque due to the charge separation self-consistently [21]. The simulation reproduced the toroidal rotation driven by the radial current from the PERP-NBI. The analysis with varying vertical injection angle (poloidal angle) indicates that the horizontal NBI drives the toroidal rotation most efficiently.

4.4. Studies on Energetic Particles and Disruption

4.4.1. Ion Cyclotron Emission due to DD Fusion Product

The ion cyclotron emissions (ICEs) due to ^3He -ions ($\text{ICE}(^3\text{He})$) and T-ions ($\text{ICE}(\text{T})$) are studied to understand the mechanism of the wave excitation. The fundamental $\text{ICE}(^3\text{He})$ was only observed in plasmas with the line averaged density less than $1.3 \times 10^{19} \text{ m}^{-3}$. The second-harmonic $\text{ICE}(^3\text{He})$ was observed in plasmas with higher density region than that for the fundamental mode, while it also disappeared at the density higher than $3 \times 10^{19} \text{ m}^{-3}$. The wave numbers of the second harmonic $\text{ICE}(^3\text{He})$ and the fundamental $\text{ICE}(\text{T})$ are evaluated as around 4 and 8 m^{-1} , respectively. The observed density dependence and wave numbers are consistent with the dispersion relation of the magneto-acoustic wave in D-plasmas with minority ^3He -ions. The fact that the wave number of $\text{ICE}(\text{T})$ was longer than that of $\text{ICE}(^3\text{He})$ indicates that the excitation of slow Alfvén waves is the mechanism for $\text{ICE}(\text{T})$ [22].

4.4.2. Current Decay Time during Disruption

The plasma current decay time during initial phase of the density limit disruption is investigated based on the plasma inductance and resistance evaluated by the experimental data. The electron temperature profile during the current quench is measured with the ECE diagnostic and with the ratio of He I line emission intensity. The plasma inductance is estimated by the Cauchy-Condition Surface method with magnetics. It is found that the time change rate of the plasma inductance during current quench is an important parameter as well as the plasma resistance to predict the current decay time [23].

5. Studies on H-mode and Pedestal Physics

5.1. Properties of Heat Transport in ELMy H-mode Plasmas

The effect of current density profile on the heat transport and edge pedestal performance is investigated in JT-60U. H-mode plasmas with higher l_i due to the current ramp down show

higher energy confinement with higher density [24]. The H-factor evaluated for the core plasma ($H_{89\text{core}}$) depends strongly on l_i with the relation of $H_{89\text{core}} \propto l_i^{0.77}$ for the case without sawtooth activities. Center peaked profiles of n_e and T_e are obtained in H-mode plasmas with high l_i . While the peripheral current density profiles are largely modified by the current ramp, the pedestal pressure is not significantly changed. The higher energy confinement in H-mode plasmas with high l_i is attributed to the core improvement with the peaked profiles of n_e and T_e , while no explicit difference in pedestal profile is observed. The electron heat diffusivity is reduced at the plasma core in high l_i case, resulting in the center peaked T_e profile while the T_i profiles are approximately unchanged.

5.2. Properties of Density Profile in ELMy H-mode Plasmas

The peaked density profile is suitable to obtain higher plasma performance as discussed before, the density profiles in LHD heliotron and JT-60U tokamak plasmas are compared in terms of the collisionality. Clear differences and similarities of characteristics of density profiles have been found between the two plasmas. The density peaking factor increased with decreasing the collisionality in JT-60U [25, 26]. In plasma having higher density peaking with higher NB power, the radial correlation length measured with the correlation reflectometer became longer in JT-60U [26].

5.3. Properties of Pedestal Structure

Previous empirical scalings of the pedestal width (Δ_{ped}) include pedestal β and/or ρ^* dependence [27]. In order to separate these two parameters, experiments in hydrogen and deuterium plasmas were performed in JT-60U. As shown in Fig. 10, the log-linear regression analysis indicates the scaling expressed as $\Delta_{\text{ped}} = 0.315a\rho_{\text{pol}}^*{}^{0.2}\beta_{\text{pol}}^{0.5}$ [28]. It is confirmed that the pedestal data in the I_p ramp experiments described in Sec. 5.1 follows the same scaling. The pedestal pressure increases with increasing the total pressure and triangularity, which is observed in both plasmas with and without ITB [18].

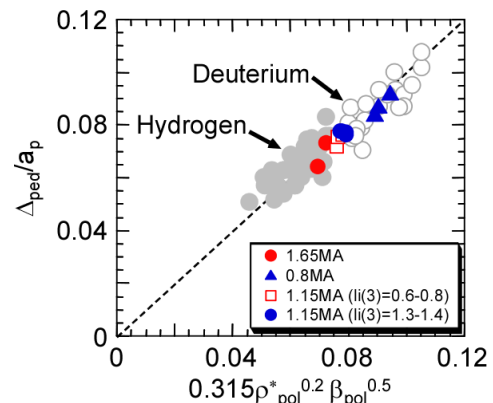


FIG. 10. Comparison of pedestal width scaling and measured width.

As discussed in Section 5.4, the width of density pedestal is typically smaller than that of the temperature pedestal. Therefore, the mechanism to determine the width of density pedestal is important. In order to understand the effect of neutral on the pedestal characteristics, three-dimensional version of the DEGAS Monte-Carlo code has been used to analyze JT-60U H-mode plasmas. The simulation results show that the increase of edge pedestal density causes a noticeable reduction of $1/e$ scale length of the neutral penetration. Consequently, the neutral penetration depth decreases with increasing the density pedestal width, which leads to the localization of ionization area near the edge pedestal region [29].

5.4. Fast Dynamics of Type I and Grassy ELMs

In order to understand the physics determining the ELM energy loss (ΔW_{ELM}), fast ELM dynamics of type I ELMs and grassy ELMs have been studied in JT-60U using new fast diagnostics with high spatial and temporal resolutions. The evolution of pressure profile is

evaluated for the first time by the detailed profile measurement of the density and temperature pedestals [30]. After a type I ELM crash, it is found that recovery of pedestal density is faster than that of temperature. Just before type I ELM crash, the pedestal ion pressure in co-rotating plasmas is higher than that in counter-rotating plasmas. However, their maximum gradient at the pedestal determined by the structure of the density pedestal was almost the same between co- and counter-rotating plasmas as shown in Fig. 11. The result suggests that the ELM size is determined by the structure of the plasma pressure in the whole pedestal region. As for the dynamics of grassy ELMs, the collapse of density pedestal is smaller and narrower than that of type I ELMs, as observed in the collapse of temperature pedestal. Thus, it is confirmed that both conductive and convective losses due to grassy ELMs are small.

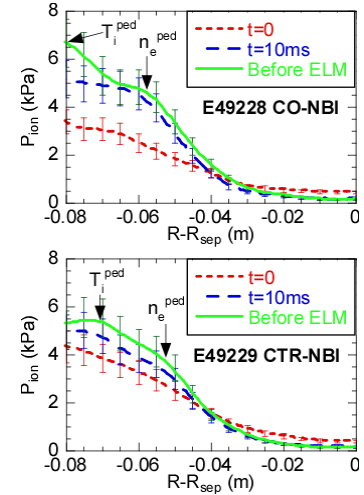


FIG. 11. comparison of ion pressure profile in CO- and CTR-rotating plasmas.

The relation between ΔW_{ELM} and ELM cycle has also been investigated using integrated modeling code, TOPICS-IB. The steep pressure gradient inside the pedestal top broadens the region of the ELM enhanced transport, resulting large ΔW_{ELM} . A transport model with the pedestal neoclassical transport connected to the SOL parallel transport reproduces the experimentally observed collisionality dependence of inter-ELM transport [31]. For constant inter-ELM transport, the ELM frequency (f_{ELM}) decreases with increasing the ΔW_{ELM} , so that the ELM loss power ($f_{\text{ELM}} \times \Delta W_{\text{ELM}}$) remains constant. Effects of a toroidal rotation on the stability of the MHD modes in the edge pedestal are also investigated numerically using new linear MHD stability code MINERVA. It is revealed that the destabilizing effect of the sheared toroidal rotation on ELMs. This destabilizing effect becomes stronger as the toroidal mode number of the unstable MHD mode increases [32].

5.5. ELM Control by Electron Cyclotron Heating at Edge Pedestal

The effect of local heating at the pedestal by ECH on ELM characteristics was investigated in terms of active ELM control. When the pedestal at the top of the plasma at high-field side was heated by ~ 1 MW EC, the f_{ELM} was increased from ~ 75 Hz to ~ 120 Hz. No response was observed, when the pedestal at the top of the plasma at low-field side was heated. The increase in f_{ELM} was not due to the increase in the heating power, since the increase in the injection power of NBI by 2.2 MW (absorbed power of 1.3 MW) only changed the f_{ELM} from ~ 70 Hz to ~ 85 Hz. With the increase in f_{ELM} , the ΔW_{ELM} was reduced by $\sim 30\%$. Thus, the localized pedestal heating by ECH can be considered as a candidate for the active ELM control technique in ITER.

6. Studies on Impurity Transport, SOL/Divertor Plasmas and Plasma Wall Interactions

6.1. Impurity Generation and Transport

The generation and transport of impurities are quite important to obtain high performance plasmas. The behavior of carbon (C) and tungsten (W), which are candidates for the material of ITER divertor tile, are investigated.

6.1.1. Studies on Carbon Transport

In order to investigate the generation and the loss flux balance of C^{3+} , which contributes 60% to the total radiation power in detached divertor plasmas, the generation flux (ionization of C^{2+} and recombination of C^{4+}) and the loss flux (ionization and recombination of C^{3+}) are compared for the first time. It is found that C^{3+} is produced by the volume recombination of C^{4+} and the ionization of C^{2+} comparably [33]. In contrast, the volume recombination of C^{3+} is not detected, and the ionization flux of C^{3+} is less than 1% of the C^{3+} generation flux. Thus, the C^{3+} generation flux is higher by two orders of magnitude than the loss flux. This result suggests that another loss mechanism of C^{3+} such as transport loss from the X-point is significant.

The carbon density profiles during the ITB formation phase were compared between LHD and JT-60U. The radial profiles of carbon density are evaluated from the radial profiles of intensity of charge exchange line CVI and beam attenuation calculation based on the measured density and temperature profiles. The carbon density starts to decrease due to an outward convection in LHD, while the carbon density tends to increase due to an inward convection in JT-60U associated with the formation of ITB [16]. The convection velocity in LHD plasma is 0.5 m/s (outward), while that in JT-60U plasma is -0.2 m/s (inward). The sign difference in the convection of the impurity transport in ITB plasma would be due to the different turbulence structure driving radial flux in particle between LHD and JT-60U.

6.1.2. Studies on Tungsten Transport

Compatibility of W as a plasma facing material has been investigated in JT-60U using the W-coated outer divertor tiles (12 tiles, covering 1/21 toroidal length). It has been found that W accumulation becomes more significant with increasing the toroidal rotation in the counter-direction [33]. As shown in Fig. 12, the impurity accumulation level shows clear Z-dependence, while it does not depend on the generation flux/puffing rate. These experimental results suggest the transport of impurity plays a dominant role to determine the accumulation level. The ECH is confirmed as a method to change the transport of impurity, since no impurity accumulation was observed during ECH even in the counter-rotating plasmas.

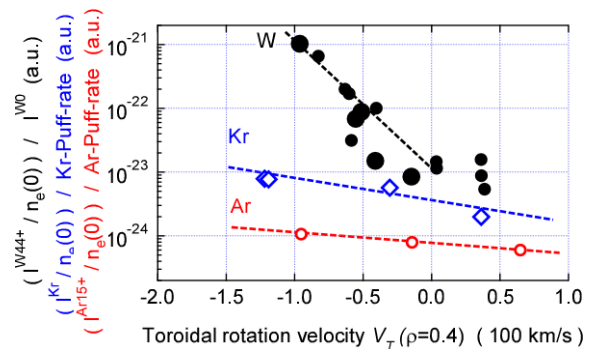


FIG. 12. Comparison of impurity accumulation between W, Kr and Ar as a function of V_T .

6.1.2. Studies on Tungsten Deposition at Divertor

Deposition profiles of tungsten released from the outer divertor were investigated. A neutron activation method was used for the first time to accurately measure deposited tungsten. Surface density of tungsten in the thick carbon deposition layer can be measured by this method. Tungsten was mainly deposited on the inner divertor (around inner strike points) and on the outer wing of the dome [34]. Toroidal distribution of the W deposition was significantly localized near the tungsten released position, while other metallic impurities such as Fe, Cr, Ni were distributed more uniformly. These data indicate that inward drift in the divertor region played a significant role in the tungsten transport in JT-60U divertor.

6.3. Fluctuation Characteristics in SOL plasmas

Detailed comparison between fluctuation characteristics at HFS and LFS scrape off layer (SOL) plasma has been made, for the first time, in L-mode plasmas using reciprocating Langmuir probes. Statistical analysis based on probability distribution function (PDF) was employed to describe intermittent (non-diffusion) transport in SOL plasma fluctuations. It was found that the positive bursting events associated with blob-like plasma transport were more frequently appeared at LFS midplane [35]. The PDF for LFS SOL plasma is strongly skewed positively, while the PDF in HFS SOL is close to Gaussian distribution. Conditional averaging analysis of the positive bursting events at LFS midplane indicates that the intermittent feature with a rapid increase and a slow decay are similar to the characteristics predicted for blobs theoretically. Statistical self-similarity was also investigated with Fourier power spectrum, and statistics of waiting-time and duration-time of the fluctuation. It was found, for the first time, that clear statistical self-similarity was observed at LFS SOLs, showing fractal property of the fluctuation. The scaling exponents disagree with the predictions for the self-organized criticality (SOC) paradigm.

7. Summary

JT-60U experiments have been focused on the further expansion of the operational regime of AT plasmas using improved flexibility of NBIs by the modification of power supply and on the investigation of important issues for the establishment of steady-state AT operation using new diagnostics and improved heating systems. In PS plasma, high $\beta_N H_{H98(y,2)}$ of 2.6 with $\beta_N \sim 2.6$ and $H_{H98(y,2)} \sim 1$ is sustained for 25 s significantly longer than the current diffusion time ($\sim 14 \tau_R$). In WS plasma, high $\beta_N \sim 2.8$ exceeding $\beta_N^{\text{no-wall}}$ is sustained for ~ 5 s with RWM stabilization by a toroidal rotation at $q = 2$ surface. In RS plasma, high $\beta_N \sim 2.7$ ($\beta_p \sim 2.3$) exceeding $\beta_N^{\text{no-wall}}$ with $q_{\min} \sim 2.4$ ($q_{95} \sim 5.3$), $H_{H98(y,2)} \sim 1.7$ and $f_{BS} \sim 0.9$ was obtained with wall stabilization. Based on PS plasma for ITER hybrid operation scenario, the high β_N of 2.1 with good thermal plasma confinement of $H_{H98(y,2)} > 0.85$ was sustained for more than 10 s at $\bar{n}_e/n_{GW} > 0.7$ and $f_{\text{rad}} > 0.77$ using stored energy feedback system and radiation feedback system. Physics studies for AT plasmas, H-mode and pedestal physics, and studies on impurity transport, SOL/divertor plasmas and plasma wall interactions are also progressed.

Acknowledgement

The authors would like to acknowledge all people who have contributed to the JT-60U projects.

References

- [1] TOBITA, K., et al., Nucl. Fusion **47** (2007) 892.
- [2] GORMEZANO, C., et al., Nucl. Fusion **47** (2007) S285.
- [3] TAKENAGA, H. and the JT-60 Team, Nucl. Fusion **47** (2007) S563.
- [4] HANADA, M., et al., Fusion Energy 2008, FT/P2-27.
- [5] MORIYAMA, S., et al., Fusion Energy 2008, FT/P2-26.
- [6] SUZUKI, T., et al., Fusion Energy 2008, EX/1-4Rc.
- [7] OYAMA, N., et al., submitted to Nucl. Fusion.
- [8] MIKKELSEN, D. R., Phys. Fluids B **1** (1989) 333.
- [9] MATSUNAGA, G., et al., Fusion Energy 2008, EX/5-2.
- [10] TOKUDA, S. and WATANABE, T., Phys. Plasmas **6** (1999) 3012.
- [11] SAKAMOTO, Y., et al., Fusion Energy 2008, EX/1-1.

- [12] ASAKURA, N., et al., Fusion Energy 2008, EX/4-4Ra.
- [13] ISAYAMA, A., et al., Fusion Energy 2008, EX/5-4.
- [14] URSO, L., et al., 35th EPS Conference on Plasma Phys. ECA Vol.32 (2008) P-2.068.
- [15] OZEKI, T., et al., Fusion Energy 2008, FT/P2-22.
- [16] IDA, K., et al., Fusion Energy 2008, EX/8-2Rb.
- [17] TAKENAGA, H., et al., Fusion Energy 2008, EX/P3-2.
- [18] KAMADA, Y., et al., Fusion Energy 2008, EX/P3-3.
- [19] YOSHIDA, M., et al., Phys. Rev. Lett. **100** (2008) 105002.
- [20] YOSHIDA, M., et al., Fusion Energy 2008, EX/3-1.
- [21] HONDA, M., et al., Fusion Energy 2008, TH/P8-15.
- [22] ICHIMURA, M., et al., Fusion Energy 2008, EX/P8-2.
- [23] OKAMOTO, M., et al., Fusion Energy 2008, EX/7-2Rc.
- [24] URANO, H., et al., Fusion Energy 2008, EX/8-5.
- [25] TAKENAGA, H., et al., Nucl. Fusion **48** (2008) 075004.
- [26] TANAKA, K., et al., Fusion Energy 2008, EX/P5-6.
- [27] HATAE, T., et al., Plasma Phys. Control. Fusion **42** (2000) A283.
- [28] URANO, H., et al., Nucl. Fusion **48** (2008) 045008.
- [29] NAKASHIMA, Y., et al., Fusion Energy 2008, EX/P6-5.
- [30] KOJIMA, A., submitted to Fusion Energy 2008 as postdeadline paper.
- [31] HAYASHI, N., et al., Fusion Energy 2008, TH/P9-14.
- [32] AIBA, N., et al., Fusion Energy 2008, TH/P9-12.
- [33] NAKANO, T., et al., Fusion Energy 2008, EX/P4-25.
- [34] UEDA, Y., et al., Fusion Energy 2008, EX/P4-16.
- [35] OHNO, N., et al., Fusion Energy 2008, EX/P4-18.